

# Optoelectronic Properties of Nanocrystalline Silicon-Based Superlattice Structures



Pratima Agarwal and Asha Yadav

**Abstract** Superlattice structures consist of alternate layers of two different materials, each having a fixed thickness. These structures thus have an additional periodicity along the growth direction and thus behave like a quasi-crystal with a periodicity much larger than that in single-crystal materials having a periodicity of the order of lattice constant of crystal and exhibit several interesting phenomena. The optical, electrical and other physical properties of these structures are significantly different from those of individual layers. In the present article, we present some interesting experimental results observed for nc-Si/a-Si:H-based superlattice structures. Though the lattice constant and electron affinity of nc-Si/a-Si:H are nearly matched, their structural, electrical and optical properties are significantly different. Our studies show that the electrical transport properties of these structures can be tuned by controlling the thickness of the individual layer. The superlattice structures with thick individual layers show excess conductivity in dark after exposure to light. On the other hand, strong photoluminescence (PL) signal in the visible range is observed for the structures with thin individual layers and the PL peak energy depends upon the thickness of the nc-Si layer. The nc-Si/a-Si:H superlattice structures can be used for silicon-based photonic devices in the integrated circuits.

## 1 Introduction

Superlattice structures are a new class of materials, which consists of alternate layers of two different materials each having a fixed thickness. The unit building block of these superlattice structures is a set of two layers, and the structure is formed by periodically repeating this building block along one direction (Fig. 1). The structures thus behave as quasi-crystal with a periodicity which is much larger than the lattice constant of the individual layer. The two layers in these materials are typically a few nanometers thin along the direction of the superlattice growth, whereas in the

---

P. Agarwal (✉) · A. Yadav

Department of Physics and Center for Energy, Indian Institute of Technology Guwahati, Guwahati 781039, India

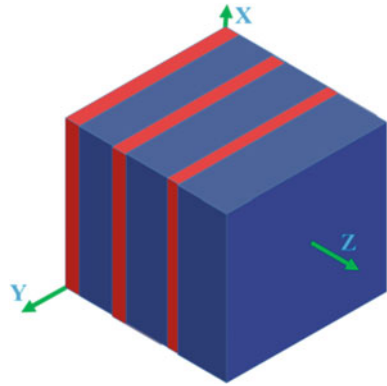
e-mail: [pratima@iitg.ac.in](mailto:pratima@iitg.ac.in)

© Springer Nature Singapore Pte Ltd. 2020

S. Kumar and D. K. Aswal (eds.), *Recent Advances in Thin Films*, Materials Horizons: From Nature to Nanomaterials, [https://doi.org/10.1007/978-981-15-6116-0\\_9](https://doi.org/10.1007/978-981-15-6116-0_9)

245

**Fig. 1** Schematic of a superlattice structure



other two dimensions these could be infinitely large (a few mm or cm). This way, the transport of charge carriers is anisotropic and the electrical properties can be tuned by choosing the thickness of the individual layer. The optoelectronic properties of these quasi-crystals are very different than those of individual layers. These structures have attracted the attention of both the theorist as well experimentalist due to their unique and tunable properties.

The semiconductor superlattice structures can be divided into two classes, (i) Compositional superlattice (heterogeneous) structures, where the alternate layers are made of two different semiconductors, having different band gaps, electron affinity, etc. and (ii) doping-modulated (homogeneous) structures, where the individual layers are differently doped semiconductor (variation in dopant type or doping concentration), for example, n-p-n-p-... , n-i-n-i-... or p-i-p-i.. structures. In the first case (heterogeneous structures), the conduction and valance band edges are discontinuous at the interface, whereas in the other case (homogeneous structures), though there is a band bending at the interface, both  $E_c$  and  $E_v$  remain continuous. In both cases, a potential well/potential barrier structure for carriers is formed. Most of these structures are fabricated using semiconductors having nearly similar lattice constant thus avoiding the interfacial strain and defects, which influence the carrier transport. A number of superlattice structures have also been fabricated with the amorphous semiconductor to study their transport and optical properties.

The superlattice structures have attracted the attention of both theorists and experimentalists due to their unique and tunable properties. The theoretical studies on compositional superlattice semiconductors have predicted many interesting phenomena such as Wannier stark hopping, sequential and resonant electron tunnelling, Bloch oscillations, Fabry–Perot Oscillations, enhanced conductivity and metal–insulator transition [1–7].

Doping-modulated superlattice structures (homogeneous), consisting of periodically varying the dopant type or concentration, such as n-i-p-i.. or n-p-n-p structures have also been studied both theoretically as well experimentally [8–10]. Such superlattice structures are free from band discontinuity at the interface. Some other interesting experimental phenomena observed for these semiconductor superlattice

structures include the persistent photoconductivity [10–12], tunable visible photoluminescence [13, 14] and electroluminescence [14, 15], tunable absorption coefficient [16] which arise due to spatial separation of electrons and hole, carrier confinement and spatially modulated energy band gap. Semiconductor superlattice structures have also been proposed as semiconductor parametric oscillators for sub-terahertz and terahertz radiation source [17], mid-infrared detector [7], infrared screen projector system [18]. Most of these studies are performed on III-V compound superlattice structures such as GaAs/GaAlAs, InAs/GaSb.

In addition to semiconductor superlattice structures, similar periodic structures could also be formed using alternate layers of materials of different refractive index or alternate layers of materials having different elastic constants. All these structures exhibit interesting optical, mechanical and electronic properties, which include extremely high carrier mobility, enhanced optical properties, high photosensitivity, low thermal conductivity, high transmittance, etc. which can be tuned by carefully choosing the thickness, band gap, doping or refractive index of the constituent layers. The superlattice structures made of different refractive index layers are used as Dielectric Bragg Mirrors [19] and exhibit photon equivalent of Bloch oscillations of electrons in the crystal lattice. Another interesting superlattice structure made of alternate metal and insulator layers has been proposed for high-speed transistor [20, 21]. Metal–semiconductor superlattice structures have also been proposed as thermionic refrigerators for integrated cooling of optoelectronic devices [22, 23].

With the advancement of the thin-film technology, which allows the growth of an atomically smooth thin layer of materials, it is possible to fabricate such multilayer structures with high precision for high-speed optoelectronic and photonic devices. A number of techniques are used to fabricate such structures such as molecular beam epitaxy, co-evaporation and co-sputtering, Pulsed laser deposition, radio frequency-Plasma Enhanced Chemical Vapour Deposition (rf-PECVD), hot wire chemical vapour deposition (HWCVD), low-pressure CVD, ion implantation, etc. Using these techniques, it is possible to fabricate semiconductor superlattice structures showing desirable optoelectronic properties, by carefully choosing the composition, doping profile and thickness of individual layers. The variation in one or more of these parameters changes the width or height of the potential well and the optoelectronic properties can be tuned due to carrier confinement and spatial separation of electron and holes in different layers. In these structures, the electron transport is anisotropic and optoelectronic properties are very different when measured in a direction, parallel or perpendicular to these layers. It is also possible to tailor the effective refractive index and optical transmission and reflection of these structures as well as the absorption coefficient.

In the past two decades, a lot of research efforts are focused on semiconductor nanostructures due to their tunable optoelectronic transport and luminescent properties. Among these, nanostructures made of silicon such as porous silicon and ultrathin nanocrystalline silicon films, are particularly of more interest because they exhibit visible photoluminescence. Bulk silicon is an indirect band gap material with an energy band gap of 1.1 eV, and thus exhibits a very poor luminescence signal in the infrared range, which restricts its use in photonics industries in spite of being the

most favourite material for the microelectronics industry and solar cell industry. The efficient visible photoluminescence in porous silicon prepared by electrochemical etching [24], suggested that it is possible to make silicon-based photonic devices if the size of the Si crystal is reduced significantly to the nano-dimension level. Other Si nanostructures have also shown photoluminescence in the visible range of electromagnetic spectra [14, 15, 25, 26]. The reduction in the size of Si crystals not only increases the band gap of Si but also relaxes the k-selection rule allowing the direct band to band transition. The peak emission wavelength of these transitions can be controlled by controlling the size of the Si nanocrystals. This discovery of light emission from nc-Si is an important breakthrough in the scientific research community since it has opened a new possibility of synthesis of Si-based light-emitting electronic devices. Si nanocrystals offer a viable pathway for the fabrication of direct band gap materials with tunable band gap depending upon the size of the Si nanocrystallites. Various methods have been employed to produce ultra-fine silicon nanocrystals such as low-pressure chemical vapour deposition, laser ablation, electrochemical anodization, rf-magnetron sputtering, rf-PECVD, microwave CVD, gas-phase synthesis, etc.

Another method to produce Si nanocrystals with the controlled size is by fabricating multilayer structures such as a-Si/SiO<sub>2</sub>, nc-Si/SiO<sub>2</sub>, Si/SiO<sub>2</sub>, etc. in which a very thin layer of Si is sandwiched between two layers of other materials such as SiO<sub>2</sub> or SiN<sub>x</sub> [14, 25, 27]. The entire structure is subsequently annealed at high temperature to form Si nanocrystals embedded in an amorphous matrix. In such structures, SiO<sub>2</sub> acts as a good size controlling layer, however due to large band offset between Si and SiO<sub>2</sub>, which influences the carrier transport, this is not a very suitable material for device application. A superlattice structure with lower band offset such as a-Si:H/nc-Si:H is desirable to increase carrier mobility for high-speed thin-film transistors. Large photocurrent enhancement is also reported in these a-Si:H/nc-Si:H superlattice structures [16]. The optical absorption enhancement from photonic and plasmonic effects has also been reported by several groups in the nanostructured a-Si:H and nc-Si:H thin film [16].

In the present article, we present some interesting experimental results observed for nc-Si/a-Si:H-based superlattice structures [13, 28, 29]. We have chosen this system because it is easier to fabricate these structures by tuning the deposition parameters in an rf-PECVD or HWCVD system. Further, the lattice constant and electron affinity for the two layers are nearly matched, though their optical absorption and electrical conductivity could be very different. The presence of atomic hydrogen during the deposition of such structures passivates the interfacial and coordination defects. These structures have shown nanophotonic and nanoplasmonic enhancements in thin-film silicon solar cells [16]. The article also includes a brief discussion on the band structure, electronic transport and optoelectronic properties of semiconductor superlattice structure and dielectric superlattice structures.

### 1.1 Electronic Band Structure and Electrical Transport in Superlattice Structures

Figure 2 shows the conduction and valence band bending for a number of heterogeneous semiconductor junctions. When a superlattice structure (Fig. 3a) is fabricated using these heterogeneous semiconductors (composition modulated semiconductor superlattice structures), the band bending and charge accumulation may vary depending upon the band gap and electron affinity of the two semiconductors. In these structures, the carriers are confined in the narrow regions and if the widths of the constituent layers are comparable to the electron mean free path, the entire electron system may behave as a quantum system in presence of nearly ideal interfaces.

In case of compositional superlattice structures, the alternate layers of low and high band gap materials impose an additional periodic potential with a period much larger than that of the lattice potential. The conduction band energy diagram for a free electron appears to be similar to the periodic potential seen by an electron in the crystal lattice, with the lattice constant  $a$  being replaced by the periodicity  $d$  of the superlattice. The periodic spatial variation of  $E_c$  in these superlattice structures results in the formation of energy bands (mini bands) in the conduction band having width and separation as shown in Fig. 3b. The energy width  $\Delta$  of these mini bands

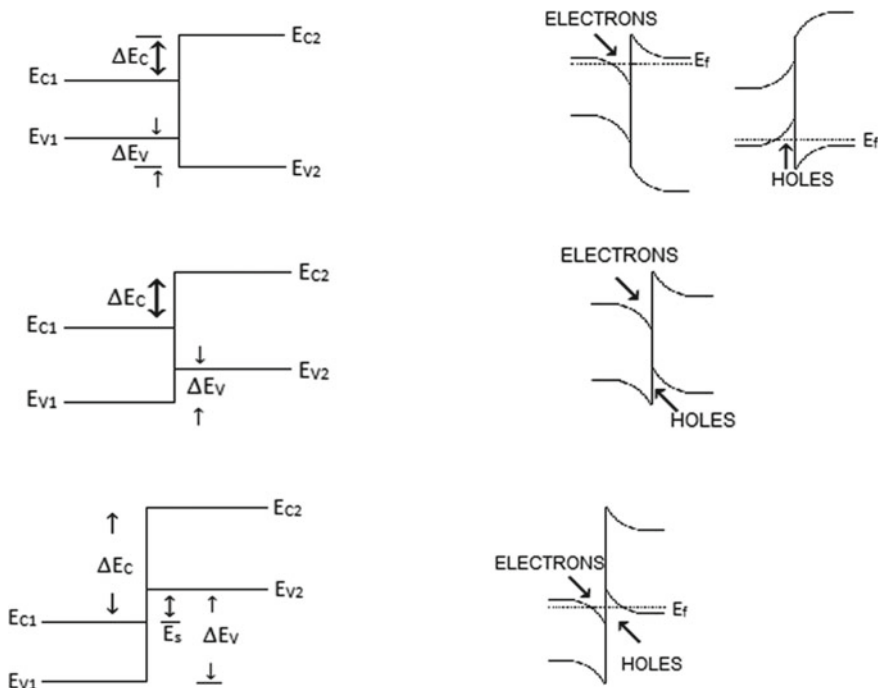
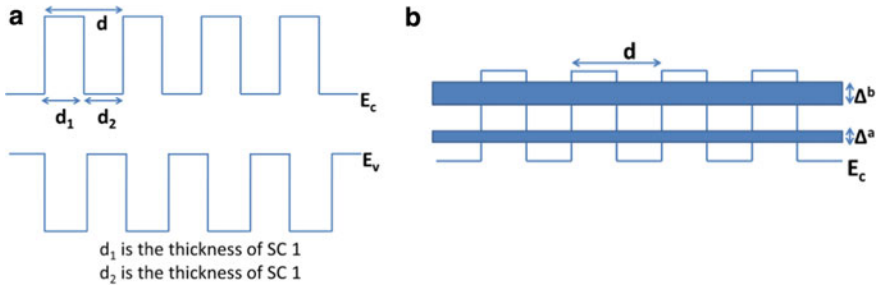


Fig. 2 Band bending at the junction of two different semiconductors



**Fig. 3** **a** Schematic compositional superlattice structure, **b** formation of minibands in conduction band in these compositional superlattice structures

and the extension  $2\pi/d$  of Brillouin zone in case of superlattice structure are now much smaller than the bandwidth and  $2\pi/a$ , the extension of Brillouin zone in the crystal lattice as lattice constant  $a \ll d$ , the periodicity in superlattice structure. Also as  $d \gg a$ , the Bloch Oscillations time ( $\sim h/eEd$ ) is much smaller compared to the corresponding scattering time ( $h/eEa$ ) in crystal lattice, where  $E$  is the external electric field. The thickness of individual layers govern the band structure and thus the electron transport and mobility of charge carriers.

When an external electric field is applied to the superlattice structures along the  $z$ -direction, the conduction band and minibands in these structures bend the same way as  $E_c$  and  $E_v$  for any semiconductor, as shown in Fig. 4. and electric current flows through it along the direction of the electric field. The magnitude of the current is determined by the band structure of the semiconductor, scattering process, external electric field strength as well as equilibrium carrier distribution. For low electric field, the current is linearly proportional to the electric field, however, when the field is high, the scattering processes may dominate resulting in the non-linear variation of current with applied electric field and phenomenon such as Wannier stark hopping and sequential tunnelling are observed [1–3].

In case of homogenous/doping-modulated superlattice structures, such as p-n-p-n layers, the band diagram is slightly different than what is discussed above. The most important feature of these structures is that the band edges are continuous unlike the compositional superlattice structures. The periodic variation in doping results in bending of bands as shown in Fig. 5. The interface between the individual layers is

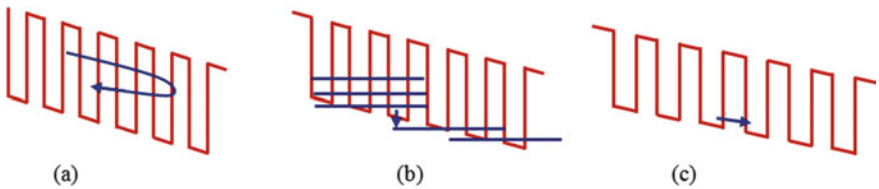
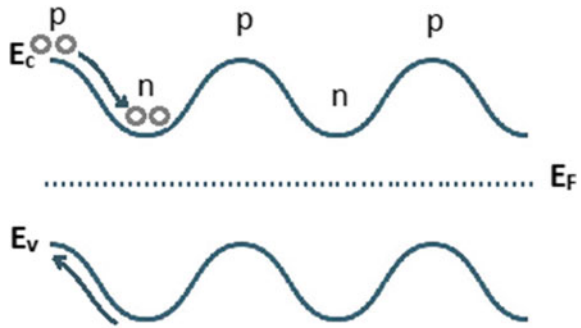


**Fig. 4** Carrier transport in superlattice structures **a** miniband conduction, **b** Wannier stark hopping, **c** sequential tunnelling

**Fig. 5** Band bending at the interfaces between doping-modulated semiconductors

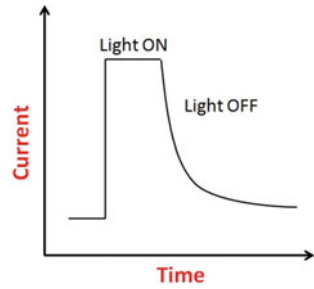


now depleted of free carriers (electrons and holes). The periodic variation in potential in such structures arise due to immobile ionized dopants in the depletion region and is electrostatic in nature, which is partially compensated by the free electrons and holes in the n- and p-doped regions, respectively. The maxima of the valence band and minima of the conduction band in such superlattice structures are spatially separated and the structures seem to have an indirect band gap in real space with the band gap value smaller than the parent semiconductor (Fig. 5). The optical band gap and optical absorption can thus be tuned by tuning the doping concentration and the period of superlattice structure. The effective band gap of these superlattice structures is smaller than that of unmodulated semiconductor material [10]. Under illumination, the photogenerated electrons and holes are spatially separated due to inbuilt potential reducing the recombination probability very significantly. It is also possible to alter the electron and hole concentration in these structures by carrier injection or extraction via an appropriate lateral electrode [9]. The photogenerated as well injected charge carriers have a very large lifetime and strong photoluminescence and electroluminescence signals are observed [16]. The structures also show interesting phenomenon such as persistent photoconductivity [10–12, 30–32].

### 1.2 Persistent Photoconductivity in Doping-Modulated Superlattice Structures

An interesting phenomenon exhibited by the doping-modulated superlattice structure is higher dark conductivity after brief exposure to illumination (Fig. 6). The phenomenon is termed as persistent photoconductivity as the current after cutting off the illumination does not fall back the equilibrium dark value instantaneously, rather decays slowly and takes a long time, a few minutes to a few hours, to return to the equilibrium dark value. The excess dark current is a fraction of photocurrent in the presence of illumination. In other words, the phenomenon suggests that in this case, recombination life time of a fraction of photogenerated electron–hole pair is enhanced which shows up as enhanced carrier concentration and thus larger current

**Fig. 6** Schematic diagram showing the PPC in semiconductors



in dark. The phenomenon has been observed for a number of superlattice structures such as doping-modulated GaAs [10, 30] and a-Si:H [12, 31, 32]-based superlattice structures. The phenomenon has also been reported for composition modulated GaAs/GaAlAs superlattice structures and some other thin films like CdS [33, 34], ZnCdSe [35, 36], CdSSe [36], ZnO [37], nanowires, porous Silicon [38], compensated a-Si:H films [31], etc. In case of doping-modulated GaAs structures, the PPC was observed at low temperature (4 K) and it persists for several hours. Whereas for a-Si:H-based doped superlattice structures, PPC was observed even at room temperature. In case of compositionally modulated GaAs/Ga<sub>0.7</sub>Al<sub>0.3</sub>As, it was observed at 4.2 K and 77 K. For GaAs, PPC is believed to arise due to spatial separation of photo-generated e-h pair as a result of band bending, which delays their recombination. In case of doping-modulated a-Si:H n-p-n-p structure, centres created by Phosphorus–Boron complexes trap the carriers, as these are in poor communication with rest of materials, and a higher current is observed after cutting off the illumination. Whereas in case of n-i-p-i structures, the holes are trapped in the acceptor like centres (AX) in the p-type regions and leave behind electrons in n-type region which results in observed PPC. The presence of dangling bonds is also believed to be responsible for the observed PPC in amorphous p-n-p-n structures. In all these a-Si:H-based superlattice structures, the observed PPC is attributed to one or more of the following: (i) presence of random local potential fluctuation arising due to compositional inhomogeneities [32], (ii) p-n junction field at the interface causing the photogenerated electron–hole pair to spatially separate before these recombine [32], (iii) presence of defect centres which capture electrons and present a barrier against the re-trapping of photoexcited carriers [12]. For several other systems, the PPC is assigned to the trapping of charge carriers in the defect states. The excess current in all these cases initially falls off rapidly followed by a slow non-linear decay. The initial rapid decay is due to the recombination of closely spaced carriers, whereas the non-linear slow decay is due to de-trapping of carriers and subsequent recombination [39].



### ***1.3 Photoluminescence in Semiconductor Superlattice Structures***

An interesting phenomenon observed for superlattice structures is tunable photoluminescence in visible and near-infrared range [40–42]. A red shift in peak emission wavelength is reported for the AlAs/GaAs superlattice structures, grown by molecular beam epitaxy, when the thickness of the GaAs layer is increased. The emission peak position for these structures is at a lower wavelength as compared to bulk GaAs. The FWHM of the main emission peak is also observed to be smaller than for bulk GaAs due to the stepwise density of states in these one-dimensional quantum wells [40, 41]. Shih et al. [40] reported two distinct peaks in the PL spectra of AlAs/GaAs superlattice structures at 4 K, which are attributed to transitions involving light and heavy holes. The position of these emission peaks shifts to a higher wavelength when the thickness of the AlAs layer is increased keeping the GaAs layer thickness constant. In these superlattice structures, essentially a periodic quantum well is formed in the GaAs layer as the band gap of AlAs is more than that of GaAs. In these structures, the carriers are confined in one-dimensional quantum well and thus its energy states are raised beyond the band gap of corresponding bulk semiconductors. The emission wavelength is controlled by controlling the width of the quantum well [40, 41]. In case of doping-modulated (Sn-doped AlAs/GaAs) superlattice structures, the PL peak energy (wavelength) is also found to depend upon the doping concentration, PL peak is blue shifted when the doping concentration is reduced [41, 42]. Photoluminescence has also been reported in Si/SiO<sub>2</sub>, Si/Si<sub>3</sub>N<sub>4</sub>, SiO/SiO<sub>2</sub>, and silicon-rich nitride/ultrathin silicon nitride superlattice structures. In all these structures, the thermal annealing at high temperatures led to the formation of nc-Si resulting in broad PL peak around 500–900 nm [14, 25, 27, 43, 44]. Tunable PL has also been observed in ZnS/ZnSe based superlattice structures [45]. It has been shown that the PL peak position depends upon the layer thickness as well as annealing temperature.

### ***1.4 Optical Properties of Dielectric Superlattice Structures***

Another interesting feature of the superlattice structures is that the optical transmission and reflection in such structures can be tuned. Figure 7 shows the propagation of electromagnetic waves through such structures. When an electromagnetic wave propagates through such structures, partial reflection and transmission takes place at each interface due to mismatch in the refractive index. The amplitude of resultant transmitted or reflected wave depends upon the reflection and transmission coefficient as well as the phase difference introduced by each of these layers. The specular reflectance and transmittance of these structures can be calculated using transfer matrix method [46–48].

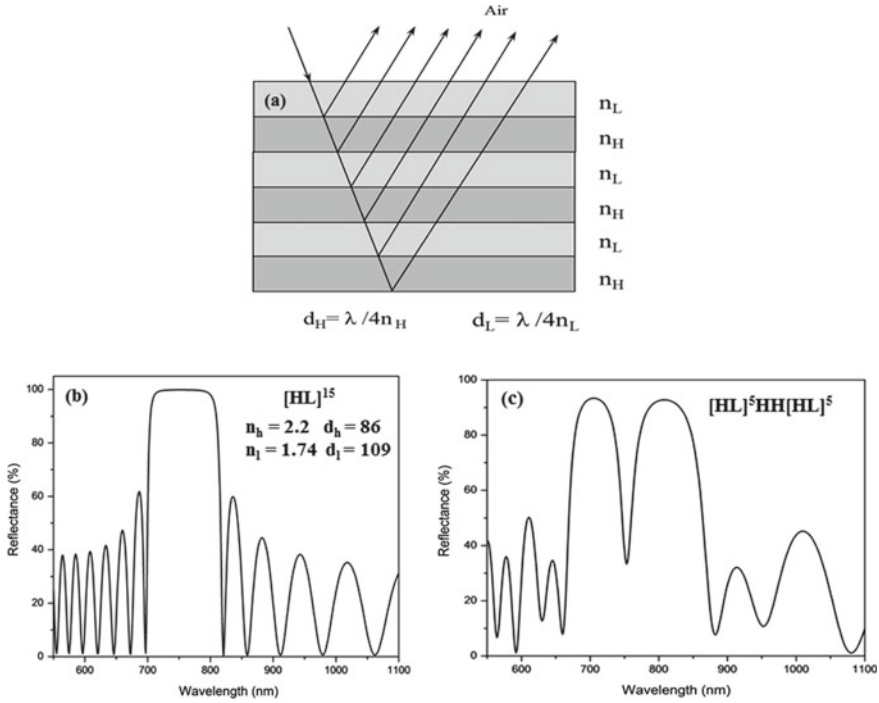


**Fig. 7** **a** Light propagation through a multilayer structure made of different refractive index layers, **b** the reflectance spectra of a 15 period multilayer structure, **c** drop in reflectance at centre of band when an extra high refractive index layer is introduced. (The refractive index, thickness of individual high[H] and low[L] refractive index layer and complete structure is mentioned in the figure) [49]

If thickness and refractive index are adjusted such that  $n_1 d_1 = n_2 d_2 = \lambda/4$ , reflectance is significantly enhanced for a narrow band around  $\lambda$ , as shown in Fig. 7 [49]. In such structures, the number of layers defines the maximum reflectance, whereas the width is controlled by the mismatch between the refractive index of two layers. Inserting an extra layer of low or high refractive index results in a sharp dip in reflectance at that  $\lambda$  (Fig. 7) and if using a femtosecond laser, the oscillations equivalent to Bloch oscillations of electrons in crystal lattice can be seen. These structures behave as one-dimensional photonic crystals and are known as dielectric Bragg mirrors. The region of high reflectance is terms as photonic band gap.

## 2 Materials and Methods

To study the electronic transport and optical properties of a-Si:H/nc-Si:H-based superlattice structures, we fabricated a number of such superlattice structures by varying the thickness of a-Si:H and nc-Si:H layers using both HWCVD and rf-PECVD techniques. The structures having thick individual layers (70 and 175 nm

each) of a-Si:H and nc-Si:H were fabricated using HWCVD techniques whereas for thin (5–30 nm) layers of a-Si:H and nc-Si:H, rf-PECVD technique is used. In HWCVD structures, the bottom layer is a-Si:H and a pair of a-Si:H layer and nc-Si layer is defined as one period. Two such structures consisting of 2 and 5 periods with 70-nm-thick individual layer and one 2 period structure with 175-nm-thick individual layers were studied in detail. The combination was chosen to study the influence of the number of layers with a thickness of individual layer at 70 nm (Case I, total thickness as well as the number of interfaces are different), and influence of thickness of each layer keeping the number of periods same (case II) and total thickness of structure constant (Case III). For rf-PECVD samples, bottom layer was nc-Si and alternate a-Si:H/nc-Si layers were deposited to fabricate the superlattice structure having an extra nc-Si layer at the top of the structure. In these structures fabricated using rf-PECVD, the thickness of nc-Si layer was varied from 5 to 30 nm, keeping the a-Si:H film thickness constant of 10 nm. Figure 8 shows the schematic of the superlattice structure fabricated by both HWCVD and rf-PECVD. These structures were deposited on Corning 1737 Borosilicate glass, undoped c-Si and ITO-coated glass substrates for different measurements. To change the microstructure of the films from amorphous to nanocrystalline silicon, hydrogen and silane flow rates were changed, which resulted in a change in the ratio of two gases. Prior to deposition of superlattice structures, single layer a-Si:H and nc-Si films were deposited to estimate the deposition rate, microstructure, and optical band gap of the films. The deposition parameters of single layer a-Si:H and nc-Si:H films prepared using HWCVD and rf-PECVD samples are listed in Tables 1 and 2. In superlattice structures, the thickness of the individual layer was varied by varying the deposition time only. The details of the thickness of individual layers, number of layers and total thickness of different structures by rf-PECVD are listed in Table 3.

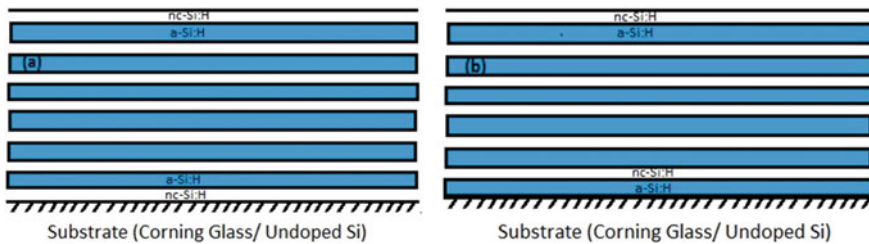


**Fig. 8** Schematic of a-Si:H/nc-Si:H superlattice structures **a** rf-PECVD and **b** HWCVD

**Table 1** Deposition parameters of single layer of a-Si:H and nc-Si:H thin films prepared using HWCVD technique [28]

Sample no.	P.P (mbar)	SFR (sccm)	HFR (sccm)	[R] (%)	$T_s$ (°C)	$T_f$ (°C)
a-Si:H	0.02	2.7	1	27	200	1900
nc-Si:H	0.2	2.6	15	85		

**Table 2** Deposition parameters of single layer of a-Si:H and nc-Si:H thin films prepared using rf-PECVD technique (P.P is process pressure, SFR (sccm) and HFR (sccm) refer to silane and hydrogen flow rates in standard cubic centimetre per min, R is the hydrogen dilution( $[\text{H}_2]/[\text{H}_2] + [\text{SiH}_4]$ )) [13]

Type	P.P (mbar)	SFR (sccm)	HFR (sccm)	[R] (%)	rf power (W)	$T_s$ (°C)
a-Si:H	0.76	8	10	55	80	250
nc-Si:H	0.68	4	96	96		

**Table 3** Deposition parameters of a-Si:H/nc-Si:H superlattice structures thin films using rf-PECVD technique

Sample no.	Thickness (nm) nc-Si/a-Si/total	No. of individual layers nc-Si:H/a-Si:H
PE99	5/10/50	4/3
PE115	10/10/70	4/3
PE137	20/10/110	4/3
PE138	30/10/150	4/3
PE93	20/10/170	6/5

Single-layer films were characterized using X-ray diffraction (XRD) and transmission electron microscope (TEM) to confirm that films are amorphous or nanocrystalline. The microstructure of the films was also confirmed by micro Raman spectroscopy. The band gap of single layer a-Si:H and nc-Si:H was estimated using the Tauc plot from UV–Vis–NIR transmission spectra and the thickness of films were measured using surface profilometer of single-layer films. Electrical characterizations, such as dark and photoconductivity, activation energy were performed on these single-layer films using Ag paste as electrodes in coplanar geometry. The PPC studies were also performed in coplanar geometry, whereas to estimate the density of states (DOS), space-charge-limited current (SCLC) measurements were performed on (ITO/a-Si:H/Ag) and (ITO{a-Si:H/nc-Si:H}<sub>n</sub>/Ag) in transverse geometry. Keithley 2450 source metre was used for these measurements and 100 W halogen lamp was used for illumination. The photoluminescence measurements were carried out using diode-pumped solid-state laser at an excitation wavelength of 405 nm and laser power 30 W. All these details are given elsewhere also [28, 29, 50].

### 3 Results and Discussion

#### 3.1 Single-Layer a-Si:H and Nc-Si:H

The XRD pattern of Si thin films prepared at different hydrogen dilution of silane [R] using both techniques (rf-PECVD and HWCVD) is shown in Fig. 9. The XRD pattern was recorded using CuK $\alpha$  radiation ( $\lambda = 1.54 \text{ \AA}$ ) in the scanning range from 10 to

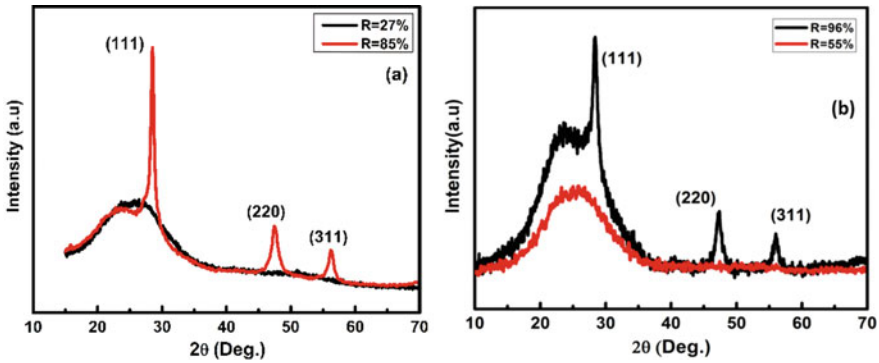


**Fig. 9** The XRD pattern of single-layer a-Si:H and nc-Si:H thin films **a** HWCVD [28] and **b** rf-PECVD [13]

70°. For both deposition techniques, the films deposited at low hydrogen dilution are amorphous in nature with a broad peak around 28°. As hydrogen dilution is increased, sharp peaks corresponding to (111), (220) and (311) planes of crystalline silicon appeared. We observed a strong peak at  $2\Theta = 28^\circ$  in both cases and less intense peak at  $2\Theta = 45^\circ$  and  $2\Theta = 56^\circ$ . These results indicate that the crystallites have a preferable orientation in  $\langle 111 \rangle$  direction for nc-Si films.

To further confirm the microstructure and calculate the fraction of the nanocrystalline phase, the Raman scattering spectra (Fig. 10) were recorded for these films using ‘Ar-ion laser’ with excitation wavelength, 488 nm, in the scanning range of  $300\text{--}600\text{ cm}^{-1}$ . In order to avoid any possibility of laser-induced crystallization [51], the low laser power density ( $\sim 127\text{ kW/cm}^2$ ) was used. The films (both HWCVD as well as rf-PECVD) prepared at low [R] show the broad peak centred at  $480\text{ cm}^{-1}$  corresponding to the transverse optic mode (TO) of amorphous silicon, whereas films prepared at higher [R] show sharp peak near about  $520\text{ cm}^{-1}$  corresponding to TO mode of phonon vibration of c-Si in both cases. To estimate the crystalline volume

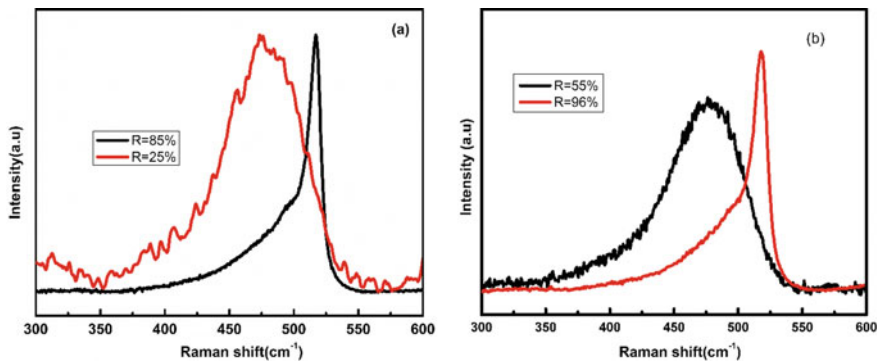


**Fig. 10** Raman spectra of single-layer a-Si:H and nc-Si:H thin films **a** HWCVD and **b** rf-PECVD

fraction in the nc-Si films, the Raman peaks were deconvoluted in three components; two Gaussian (at  $480\text{ cm}^{-1}$  and  $495\text{ cm}^{-1}$  corresponding to TO mode of a-Si:H and grain boundaries respectively) and one Lorentzian peak (at  $511\text{ cm}^{-1}$  corresponding to nc-Si) as described elsewhere [51]. The estimated total crystalline volume fraction for nc-Si films deposited by both techniques is about 64%.

The optical band gap was estimated from UV-Vis-NIR transmission spectra of thick single layer a-Si:H (110 nm) and nc-Si:H (95 nm) film prepared using rf-PECVD and was found to be 1.8 and 2.1 eV, respectively, while for the HWCVD films, the band gap was found to be 1.9 and 2.1 eV for a-Si:H (160 nm) and nc-Si:H (410 nm) films. Dark and Photo Conductivity measurement at room temperature in coplanar geometry were also performed to estimate the photosensitivity of these films. The amorphous films (deposited at lower hydrogen dilution) showed high photosensitivity of 4 order in magnitude, whereas, nc-Si films (deposited at higher [R]) showed low photosensitivity of  $\sim 1$  order in magnitude, which is the characteristic features of amorphous and nanocrystalline silicon thin films. The above results confirm that with the change in  $\text{H}_2$  dilution there is a structural transition from amorphous to nanocrystalline film irrespective of the deposition techniques.

### 3.2 *Persistent Photoconductivity (PPC) on Nc-Si/a-Si:H Superlattice Structures*

As discussed in Sect. 1.2, persistent photoconductivity (PPC) is an interesting phenomenon observed in a number of superlattice structures as discussed above. In PPC, current does not fall back to initial dark value after switching OFF the illumination, instead it shows a slow exponential decay. In this section, a detailed study on persistent photoconductivity in a-Si:H/nc-Si:H superlattice structures (where none of the layers is doped) has been presented. To understand the origin of PPC in these structures, the measurements were performed to measure the extent of excess current (%PPC), PPC decay time constant and its dependence on exposure time, number of periods, individual layer thickness and lateral electric field in superlattice structures. The measurements were performed on both thick and thin layer structures fabricated using HWCVD and rf-PECVD techniques, respectively. The electrode geometry used for these measurements is shown in Fig. 11.

Figure 12 shows the current transient for single layer a-Si:H and nc-Si films and also for three different superlattice structures under illumination and after switching off the light. All the samples have been in the as-deposited state without any post-deposition treatment. As can be seen from these figures, for all the samples, an almost instantaneous increase in current is observed as soon as the light is turned on due to excess carriers generated during illumination. The subsequent nature of the transient is, however, slightly different for different samples. For a-Si:H, a slow decay in current while the light is ON is observed followed by a rapid decrease in current to its dark value (Fig. 12a), which is known as Staebler–Wronski effect in a-Si:H.

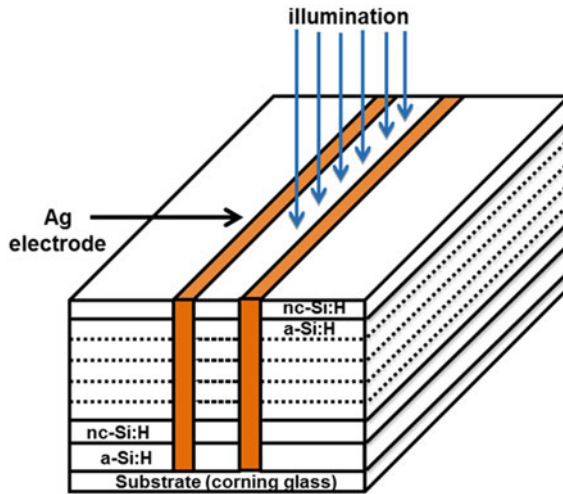


**Fig. 11** Schematic diagram of a-Si:H/nc-Si:H superlattice structure and electrode geometry [50]

For nc-Si, the current remains almost constant during illumination and decreases instantaneously to dark value when the light is OFF (Fig. 12a) showing no sign of excess current. For superlattice structures, however, the nature of this transient is quite different (Fig. 12b–d). For all these structures, an initial rapid rise in current followed by an almost linear slow increase is observed while the light is ON. When the light is OFF, the excess current after the initial rapid decrease decays slowly approaching its dark value. This nature of current transient is the same for different subsequent exposure time, and each time, the current settles to a slightly higher value than the previous stage.

The slow decay part of the photocurrent after turning OFF the illumination is well described by single exponential decay function:

$$I = I_o \exp^{-\frac{t}{\tau}} \tag{1}$$

where  $I_o$  is the pre-exponential factor and  $\tau$  is the decay time constant. The time constant for different structures and exposure times are listed in Table 4. It is observed that the decay time constant is high for the structure having more number of layers.

The PPC (%) is determined using relation as given below:

$$\text{PPC}(\%) = \frac{\Delta I_d}{I_d} \tag{2}$$

where  $I_d$  is the dark current measured just before switching ON the illumination and  $\Delta I_d$  is the excess dark current after 180 s of switching OFF the light. These values are also listed in Table 4. The PPC % is more for the structure having more number of layers.

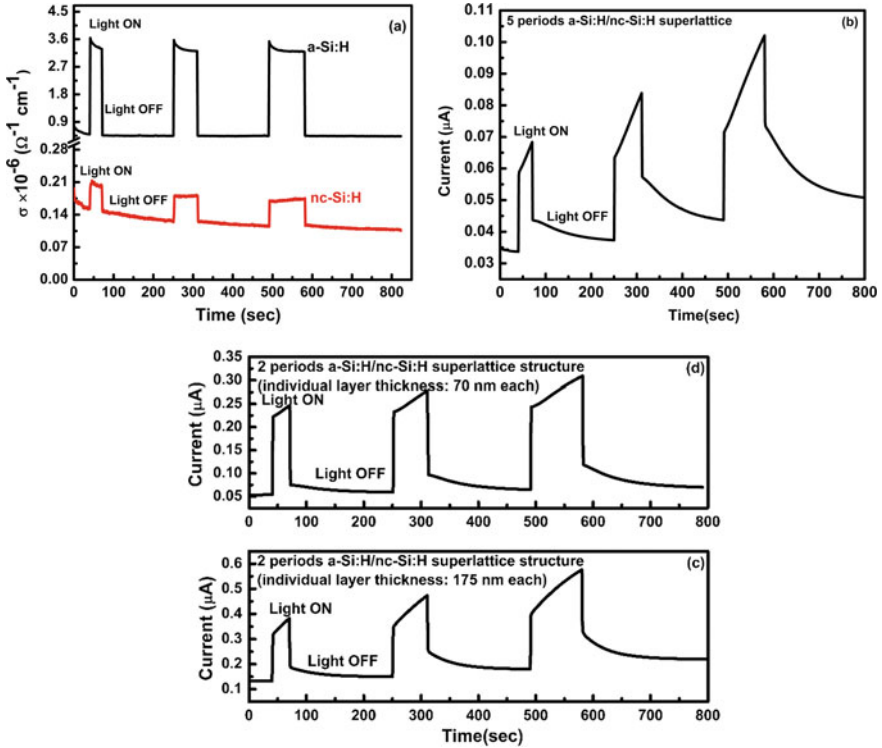


**Fig. 12** Rise and decay of photoconductivity of as deposited **a** single-layer a-Si:H and nc-Si:H thin films and rise and decay of photocurrent of **b** 5 periods (70-nm-thick each layer), **c** 2 periods (175-nm-thick each layer) and **d** 2 periods (70-nm-thick each layer) of a-Si:H/nc-Si:H superlattice [28]

**Table 4** The values of dark current, photocurrent, PPC and the decay time constant of the thick individual superlattice structures prepared by HWCVD technique [28]

Type (individual layer thickness)	Annealed temperature	$I_{\text{dark}}$ ( $\mu\text{A}$ ) at RT	$I_{\text{photo}}$ ( $\mu\text{A}$ ) at RT	$I_{\text{ppc}}$ ( $\mu\text{A}$ ) at RT	PPC (%)	$\tau$ (sec)		
						30 (sec)	60 (sec)	90 (sec)
5 periods (70 nm)	As deposited	0.03	0.06	0.04	33	91.20	80.54	76.14
	70 °C	0.29	0.52	0.35	20	45.96	45.95	46.01
	120 °C	1.77	2.45	1.93	9	47.03	47.31	47.75
2 periods (175 nm)	As deposited	0.13	0.32	0.15	15	44.20	42.70	41.80
2 periods (70 nm)	As deposited	0.053	0.220	0.059	11	69.29	67.19	64.77



The PPC has been earlier reported for a number of semiconductor superlattice structures, including doping-modulated (n-p-n-p-n-p) a-Si:H-based structures. In these doping-modulated structures, PPC is believed to be due to trapping of the carriers at the centres made by P-B complexes, which are in poor communication with the rest of the material [31]. Several models have been proposed to understand the origin of PPC in semiconductors in the past [31, 52–54]. In our case, the role of P-B complex or AX or DX is ruled out as these superlattice structures are made without any doping. Further, the extent of PPC and its decay constant is found to depend upon the number of layers and individual layer thickness. Since there is a small difference in band gap and significant difference in dark conductivity of the two layers, trapping of photogenerated charge carriers at the interface or the separation of carriers due to band bending caused by in-homogeneities thus appears to be the more likely cause of the observed PPC [28]. Also, there could be a large number of interface states present in these structures due to the presence of dangling bonds in a-Si:H and grain boundaries in nc-Si layers. In order to further understand the role of these states, the PPC measurements were carried out again at room temperature after annealing these structures at 70 °C and 120 °C, respectively. Figure 13 shows the current transient for 5 period structure after annealing. The structure was chosen as this showed the maximum PPC and largest decay time constant in the as-deposited state. The PPC% and decay time constant are listed in Table 4. It is observed that both PPC% and decay time constant decreased after annealing.

In order to further understand the origin of the observed PPC, the electric field dependence of photoconductivity (Fig. 14a) and PPC are also measured for the structure annealed at 120 °C. It is observed that the photocurrent varies linearly with the applied field; however, the extent of PPC reduces with the increase in the applied field as shown in Fig. 14b.

The observed PPC in these structures can be explained by trapping of one type of photogenerated carriers at the interface states. As a-Si:H and nc-Si have a slightly different band gap, the band bending at the interface is likely to be there. Assuming that the electron affinity for the two layers is not different, the schematic band picture

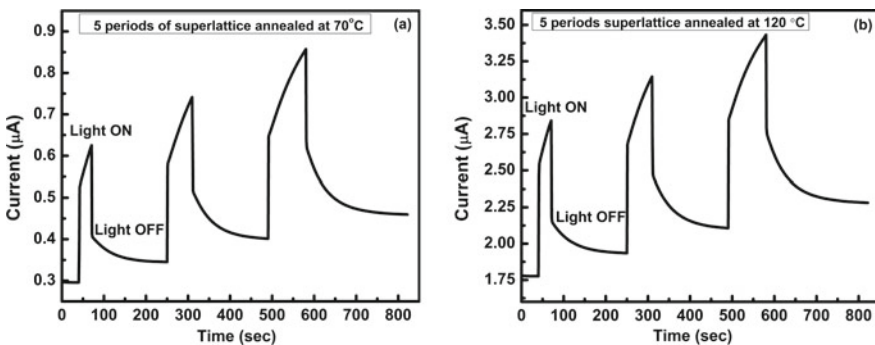


**Fig. 13** Rise and decay of photocurrent (measured at RT) of 5 periods of superlattice structure annealed at **a** 70 °C and **b** 120 °C [28]

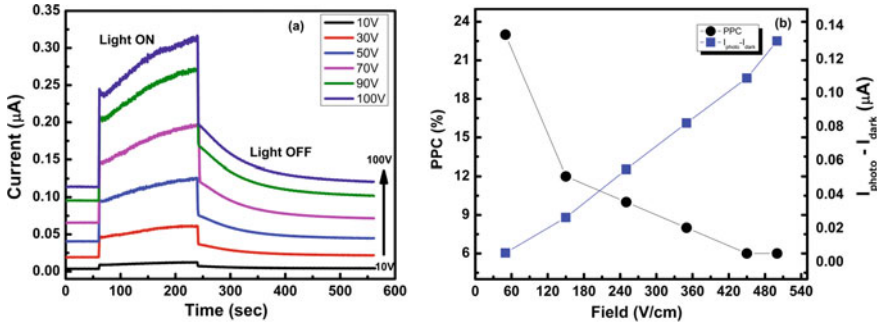


**Fig. 14** a Rise and decay of the photocurrent with the variation of external applied field, b Variation of PPC (%) and photocurrent with the change of external applied field in 5-period superlattice structures [28]

at the junction is likely to be similar to that is shown in Fig. 15. In this picture, though there is no discontinuity for the conduction band at the interface, a band discontinuity is seen for the valence band. The electrons in the nc-Si:H region can move freely to the a-Si:H region, however, the holes in a-Si:H region are likely to be trapped in the interface states. When the light is shone, the photogenerated carriers are generated, some of these carriers recombine instantaneously whereas, other drift towards the interfaces due to the field at the junction. Thus, the electrons and holes are physically separated preventing their recombination. When the light is OFF, these trapped carriers are remitted to the extended states and recombine slowly resulting in a slow exponential decay of the photocurrent. As the number of such interfaces is increased, more such carriers are trapped resulting in larger excess current (PPC) and slower decay of current. When the thickness of the individual layer is large (175 nm), more carriers are generated in a-Si:H layer and PPC % is slightly more than for structures having thin layers (70 nm) but the same number of interfaces. The model can also explain the electric field dependence of PPC in these structures. Though current is measured in lateral direction, normal to these interfaces, the photogenerated carriers are likely to move also along the interfaces due to the inbuilt field at the interfaces (Fig. 16) which may not be very high as in case of p-n junction. For a low electric field in the lateral direction, the built-in

**Fig. 15** Schematic band diagram of a-Si:H/nc-Si:H superlattice structure [28]

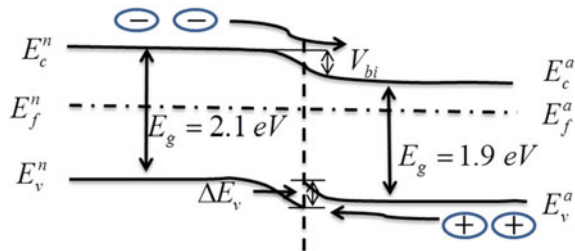
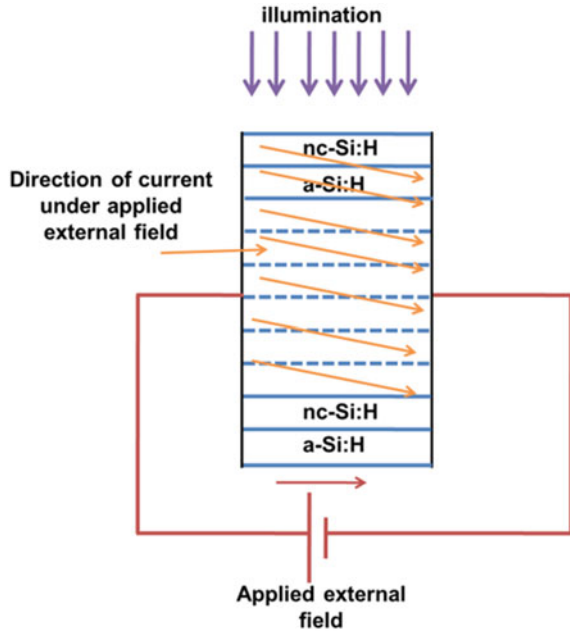


**Fig. 16** Direction of current under the applied external field in the superlattice structure [28]



field at the interfaces could be sufficiently large to drag a fraction of photogenerated carriers towards the interfaces where these are trapped, before these are swept in lateral direction. At higher lateral fields, more carriers are swept by the external field in lateral direction and the observed PPC is low. The origin of PPC is understood in terms of competition between carriers transport in the lateral direction due to the external field and along the depth due to band bending at a-Si:H/nc-Si:H interfaces. Carriers trapped in the interfaces states or the separations of carriers due to band bending are likely to be responsible for observed PPC [28].

Since both % PPC and decay time constant were found to depend on individual layer thickness also (Refer the results for 2 period structures having individual layer thickness as 175 and 70 nm each in Table 4), these studies were also conducted on the thin layer a-Si:H-and nc-Si:H-based superlattice structures prepared using rf-PECVD techniques, where individual layer thickness could be tuned to as low as 5–10 nm. This individual layer thickness is compared with the width of the band bending region at the interfaces.

Figure 17 shows the rise and decay of photocurrent for the individual layers (110-nm-thick a-Si:H layer and 95-nm-thick ncSi layer) and superlattice structures prepared using the rf-PECVD technique. For single-layer films (Fig. 17), once again, the current transient was similar to that for films deposited by HWCVD techniques and no PPC was observed either for a-Si:H or nc-Si films. However, in case of superlattice structures of 7 layers (Fig. 18a) with nc-layer thickness in the range of 5–20 nm (with the total thickness of 50–110 nm), though an increase in current was observed for all the structures (despite the total thickness being very less), the current

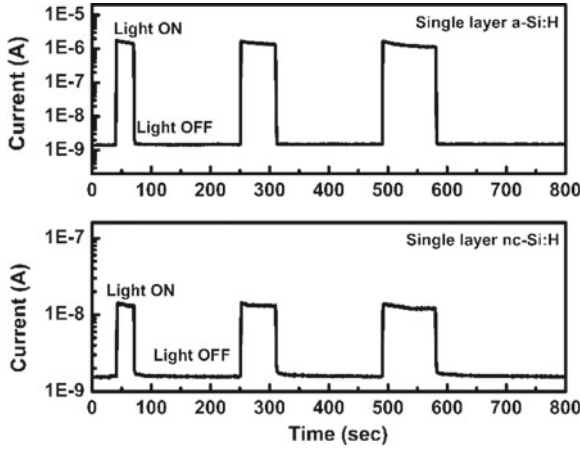


**Fig. 17** Rise and decay of the photocurrent across a single layer of a-Si:H and nc-Si:H thin films [13]

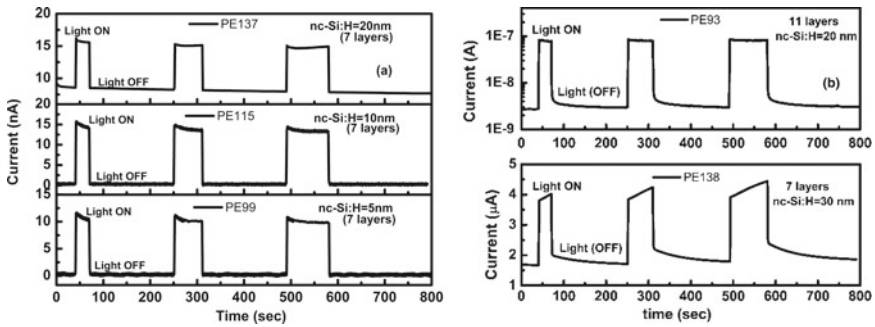


**Fig. 18** Rise and decay of the photocurrent in a-Si:H/nc-Si:H superlattice with nc-Si:H layer thickness of **a** 5 nm, 10 nm, 20 nm (7 layers) and **b** 30 nm (7 layers) and 20 nm (11 layers) structures [13]

decayed instantaneously to its dark value as soon as the light was OFF and no PPC was observed. However, in the structures with (Fig. 18b, c) nc-Si:H layer thickness of 30 nm (total thickness of 150 nm) and the superlattice structure of 11 layers with nc-Si:H layer thickness of 20 nm (total thickness of 170 nm), a slow decay of excess current was observed, after the initial rapid decrease, when the light was OFF. PPC illustrated by the appreciable excess current when the light is turned OFF (Fig. 18b, c). The values of dark current, photocurrent, PPC (%) and decay time constant for these structures are listed in Table 5.

Though the observed PPC (%) for superlattice structures having thin individual layer (rf-PECVD) is small compared to that with thick sublayers of a-Si:H and nc-Si:H films prepared using HWCVD technique, it can be seen that in this case also, PPC% increases with increase in the number of layers from 7 (total thickness of

**Table 5** The values of dark current, photocurrent, PPC and the decay time constant of the thin superlattice structures prepared by rf-PECVD technique [13]

No. of layers thickness (nm)	$I_{\text{dark}}$ ( $\mu\text{A}$ )	$I_{\text{photo}}$ ( $\mu\text{A}$ )	$I_{\text{ppc}}$ ( $\mu\text{A}$ )	PPC (%)	$\tau$ (sec)		
					30 (sec)	60 (sec)	90 (sec)
7-layer nc-Si:H 30 nm	1.67	3.77	1.71	2	67.97	69.68	72.10
11-layer nc-Si:H:20 nm	$2.72 \times 10^{-3}$	$8.22 \times 10^{-3}$	$3.0 \times 10^{-3}$	10	21.24	23.00	26.24

150 nm) to 11 (total thickness 170 nm). For 7-layer supper lattice structures, no PPC is observed when nc-Si layer is only 20 nm (total thickness of  $\leq 110$  nm) and very small PPC is observed for nc-Si layer with a thickness of 30 nm (Total thickness (150 nm). The absence of PPC for these superlattice structures with low total thickness as well as low individual layer thickness could be due to (i) insufficient absorption of light (when the total thickness is low) resulting in very few photogenerated carriers and (ii) due to possible tunnelling of carriers between a-Si:H and nc-Si:H layers when the thickness of nc-Si:H is low (5–10 nm). As the layer thickness is increased, the band bending, depletion width, and thickness of the undepleted region are likely to change. This may not allow all the carriers to tunnel through and some of these may get trapped at the interface in between a-Si:H and nc-Si:H layers resulting in observed PPC. With an increase in the number of layers, the number of such interfaces as well as total thickness increases which result in the observed PPC for 11-layer structure with 20-nm-thick nc-Si:H layers and no PPC for 7-layer structure with 20-nm-thick nc-Si:H layers [13].

### 3.3 *Space-Charge-Limited Conduction (SCLC) in nc-Si/a-Si:H Superlattice Structures*

In an earlier section, we have observed that the superlattice structures consisting of alternate layers of nc-Si and a-Si:H show PPC when current is measured in coplanar geometry normal to the direction of superlattice structures. Other studies on similar structures also report an enhancement in photosensitivity, carrier mobility and photonics and plasmonic properties [16, 55, 56]. In all these multilayer structures, the interface states between the sub-layers act as trapping and recombination centres and control the carrier transport. The role of these interface states become much more significant, if the carrier transport is along the direction in which the superlattice structures are fabricated. In addition to these interface states, the nc-Si as well as a-Si:H layers have short-range order only and are characterized by the

density of states in the band gap region. For any device fabrication, a knowledge of the density of states and interface states are very necessary.

A number of techniques have been reported to measure the density of states which include field-effect measurements [57–60], capacitance–voltage measurements [61, 62], isothermal capacitance transient spectroscopy [63], transient current spectroscopy [64], transient voltage spectroscopy [65], etc. All these transient techniques involve a complicated analysis as carriers from different trap states have different evolution times as well. Steady-state space-charge-limited current (SCLC) measurement [66–70] is a simple method of estimating the density of states as this does not involve any transient measurements and current is measured as a function of the applied field. As the carriers are trapped in the defect states, the shift in the position of Fermi level with applied field results in a non-linear variation of current, which is used to estimate the density of defect states.

In this section, we present our SCLC studies on single-layer a-Si:H and nc-Si films and nc-Si/a-Si:H superlattice structures. The HWCVD fabricated structures having thick nc-Si and a-Si:H layers (70 nm each) with two different periods (2 and 5 periods) have been used for these studies. The structures with very thin layers of a-Si:H and nc-Si could not be used for these studies as for even the smallest voltages, which could be applied from the source metre, the electric field was too large.

We used a Schottky diode configuration, *ITO (Indium Tin Oxide)/a-Si:H/Ag* and *ITO(a-Si:H/nc-Si:H)<sub>n</sub>/Ag*, for these measurements, where *ITO/a-Si:H* acted as a Schottky junction, whereas *Ag/a-Si:H* and *Ag/nc-Si:H* acted as an ohmic junction. The measurements were performed in sandwich geometry. The *I-V* characteristics in the non-linear region were used to estimate the DOS in single-layer a-Si:H and a-Si:H/nc-Si:H superlattice structures [29]. In single-layer films, the injected charge from the metal to semiconductor (Ag to a-Si:H) was trapped in the DOS in the band gap, whereas in superlattice structures, the charge redistributed itself between the defect states in the band gap region as well as at the interface between the nc-Si:H and a-Si:H layers.

Den Boer's step by step method [71]. is considered as the simplest method for estimating the DOS because in this case, the spatial variation in DOS is neglected. When the voltage difference changes from  $V_1$  to  $V_2$ , the shift in the Fermi energy level ( $E_{fn}$ ) is given as follows:

$$\Delta E_{fn} = kT \ln \left( \frac{I_2 V_1}{I_1 V_2} \right) \quad (3)$$

In the non-linear region of *I-V*, the charge density  $Q_t$  injected into the trap states is related to the change in voltage  $\Delta V = (V_2 - V_1)$  as follows:

$$Q_t = \frac{\epsilon_s \chi \Delta V}{d} = qd \int_{E_{fn}}^{E_{fn} + \Delta E_{fn}} g(E) dE = qd g(E) \Delta E_{fn} \quad (4)$$

The factor  $\chi$  accounts for the non-uniformity of the space charge and is taken as a constant ( $\chi = 2$ ),  $\epsilon_s$  is the semiconductor permittivity ( $\epsilon_s = 105.31 \times 10^{-12} \text{ Fm}^{-1}$ ; dielectric constant of silicon = 11.9),  $q$  is the electronic charge,  $d$  is the thickness of the film and  $g(E)$  is the DOS distribution in the a-Si:H film around the Fermi level.

For a sufficiently small  $\Delta V$ ,  $g(E)$  can be assumed to be constant between  $E_{fn}$  and  $E_{fn} + \Delta E_{fn}$ . From Eq. (4), the DOS is given by

$$g(E) = \frac{\chi \epsilon_s \Delta V}{qd^2 \Delta E_{fn}} \tag{5}$$

Using the values of  $\Delta V$  and  $\Delta E_{fn}$ , the distribution of the DOS can be estimated using Eq. (5).

Figures 19a, b and 20a, b show the dark  $I$ - $V$  curves in sandwich geometry for single as well as superlattice structures at room temperature (RT) after annealing it at 150 °C. For single-layer nc-Si films, the  $I$ - $V$  curve is found to be linear over the

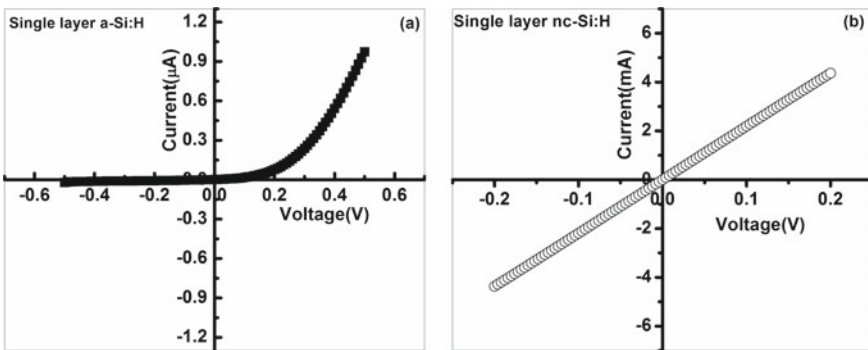


Fig. 19 I-V across single layer a a-Si:H and b nc-Si:H in sandwich geometry [29]

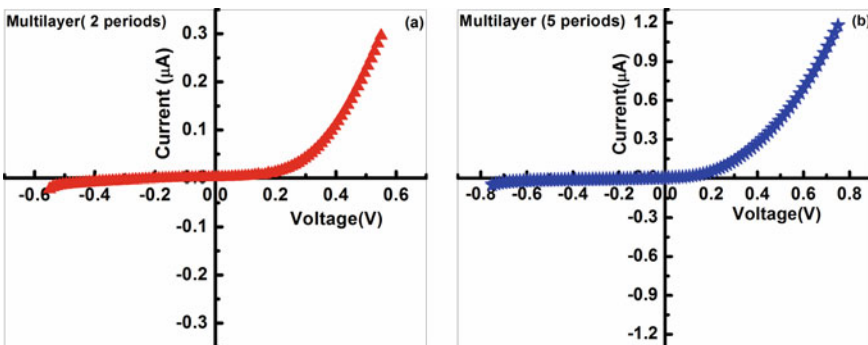


Fig. 20 I-V across total a-Si:H/nc-Si:H a 2 periods and b 5 periods superlattice structures in sandwich geometry [29]

measured range of voltage ( $4 \times 10^3$  V/cm), whereas in case of amorphous silicon films, a non-linear variation in current with voltage, with rectifying nature (ITO/a-Si:H junction is rectifying) is observed. In this case, in forward bias condition, the current increased exponentially with the applied field, with a diode ideality factor being  $\sim 2$ . The conductivity of a-Si:H and nc-Si:H in this sandwich geometry is found to be different by several orders of magnitude,  $4.3 \times 10^{-9} \Omega^{-1}\text{cm}^{-1}$  and  $1.1 \times 10^{-5} \Omega^{-1}\text{cm}^{-1}$ , respectively (Electric field  $< 1 \times 10^4$  V/cm); the dark conductivity of nc-Si:H films at 300 K is more than 3 orders of magnitude higher as compared to a-Si:H films under forward bias condition. Dark  $I$ - $V$  characteristics of a-Si:H/nc-Si:H (2 and 5 periods) superlattice structures at RT after annealing these films at 150 °C are also found to be asymmetric and non-linear similar to a-Si:H film with the diode ideality factor being  $\sim 2$  and current having the same order of magnitude as that for single layer a-Si:H film. Since the conductivity of nc-Si:H layer is much higher, where the thickness of both a-Si:H and nc-Si layer is same, it can be assumed that the nc-Si layer in these structures behave like short-circuit elements and the resistive path for carriers is only due to a-Si:H layers and the depletion region at the interface, most of it being on a-Si:H side only.

In order to estimate the density of states in the single layer of these superlattice structures, it is necessary to know the voltage drop across single layer in these multilayer structures. As nc-Si layer offers much smaller resistance (more like short-circuit element), it can be assumed that the entire voltage is dropped across a-Si:H layers. With this approximation, equivalent  $I$ - $V$  curve for one pair of a-Si:H/nc-Si:H structure in both the superlattice structures are replotted, dividing the voltage by a factor of 2 and 5, respectively, for 2 and 5 period structures, respectively. Whereas the current is same as earlier since the resistance offered by these layers are connected in series in sandwich geometry. The  $I$ - $V$  curves for single-layer a-Si:H films and across single pair of a-Si:H/nc-Si in superlattice structures on log-log scale are shown in Fig. 21. The  $I$ - $V$  curves obey power law, i.e.  $I \propto V^m$ , with different values of exponent in different regions of the curve, a characteristic of space-charge-limited conduction. The value of  $m$  for different regions is shown in Fig. 21a-c. In the low-field region, where the current is Schottky limited, the exponent is less than 1. Further for electric field  $> 10^4$  V/cm, the current increased sharply with the exponent greater than 2.0, which could be due to the onset of space-charge-limited conduction in these structures.

To estimate the shift in Fermi level (Eq. 3) and the density of state (Eq. 5), the region with  $m > 2$  of  $I$ - $V$  characteristics are used. Further, to measure the variation of DOS as a function of the shift in Fermi energy, the initial field ( $> 1 \times 10^4$  V/cm) was kept constant for the given samples. The variation of DOS with the change in  $\Delta E_{fn}$  is shown in Fig. 22a for both single as well as superlattice structures. It is observed that DOS is high for the superlattice structures than that for single layer a-Si:H film. Further, DOS does not depend on  $\Delta E_{fn}$  for single-layer a-Si:H film, however, a little variation with  $\Delta E_{fn}$  is observed for superlattice structures. The average value of DOS over the entire range of  $\Delta E_{fn}$  is also estimated from the slope of  $\Delta V$  verse  $\Delta E_{fn}$  (Fig. 22b using Eq. 5 and the values of  $g(E)$  are listed in Fig. 22b. It is observed that  $\Delta V$  verse  $\Delta E_{fn}$  curves overlap for both superlattice structures



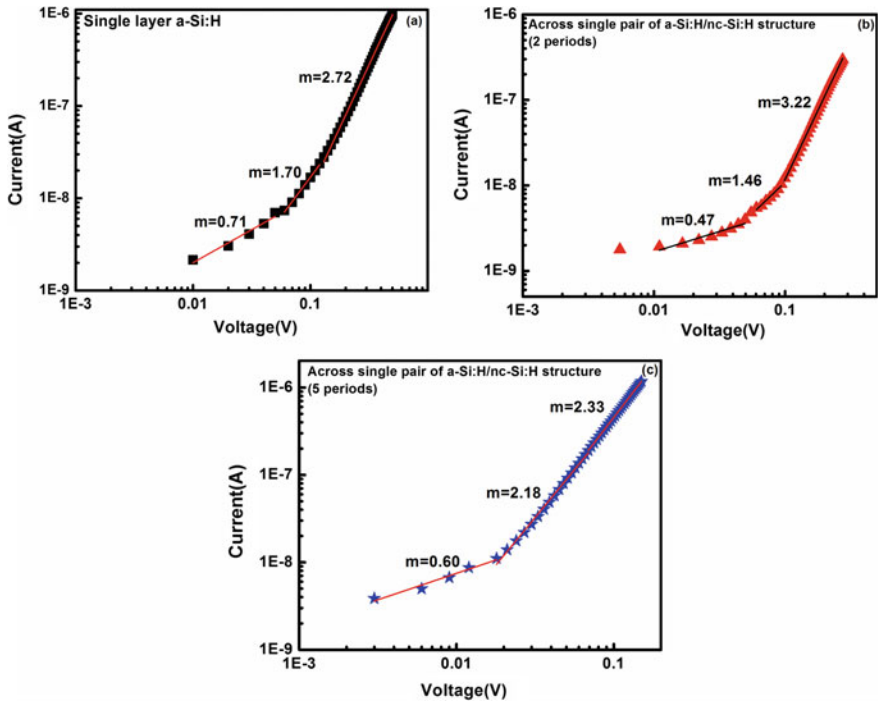


Fig. 21 I-V across a single layer a-Si:H film, across a single pair of a-Si:H/nc-Si:H b 2 periods and c 5-period superlattice structures [29]

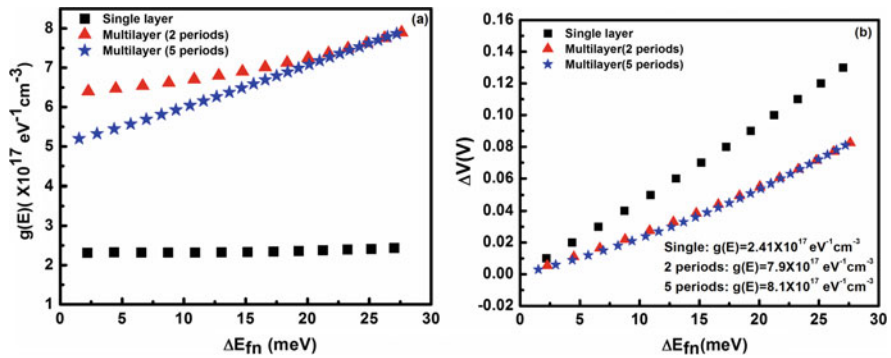
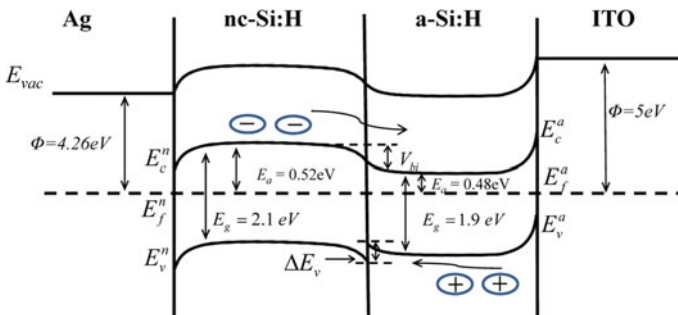


Fig. 22 a Variation of DOS and b  $\Delta V$  versus  $\Delta E_f$  across single, 2-period and 5-period superlattice structures (across single pair of a-Si:H/nc-Si:H) [29]

irrespective of number of layers. It has also been observed that the DOS obtained across superlattice structures of both the periods (2 and 5) is almost same and is higher by a factor of 5 as compared to single-layer a-Si:H film.

In our case, the DOS obtained across a-Si:H film was  $\sim 10^{17} \text{ eV}^{-1} \text{ cm}^{-3}$ , typical of a-Si:H samples, however for both the superlattice structures it was  $\sim 10^{18} \text{ eV}^{-1} \text{ cm}^{-3}$ . It may, therefore, be assumed that the observed difference in DOS in case of single-layer and superlattice films (Fig. 22a) might arise due to the presence of interface states between a-Si:H and nc-Si:H layers in these superlattice structures. These interface states are also found to be responsible for observed PPC in these superlattice structures as discussed in the PPC section.

The higher DOS in superlattice structure can be understood by drawing the equivalent band diagram and the charge transport across this. Figure 23 shows the band diagram of a-Si:H/nc-Si:H superlattice structure with ITO as the base electrode and Ag as the top electrode. In a-Si:H/nc-Si:H superlattice structure, the difference in band gaps of nc-Si:H and a-Si:H results in band bending giving rise to a built-in electric field at the interface, which controls the charge transport across the interface and affect the carrier recombination kinetics. The rectifying junction at ITO/a-Si:H interface also results in built-in electric field under no bias condition. In absence of any bias, the current density from semiconductor to ITO ( $J_{sc;ITO}$ ) must be equal and opposite of current density from ITO to semiconductor ( $J_{ITO;sc}$ ). Under the influence of external bias, which forward biases the ITO semiconductor (ITO/a-Si:H) contact, the bands in the a-Si:H side are raised in energy relative to those of ITO and the electric field at this junction decreases, therefore the charge carriers are able to cross the barrier without any obstacles, resulting in increase in  $J_{ITO;sc}$  under the applied field. If we further increase the external voltage, the bands at the ITO semiconductor junction as well as a-Si:H and nc-Si:H interface approach to become flat and thus the carrier (electrons) from nc-Si:H layer (highly conducting) to a-Si:H (low conducting) could easily tunnel towards ITO. In this process, some of the electrons get trapped in the bulk density of states of a-Si:H as well as the interface states between a-Si:H and nc-Si:H. This could be the reason behind the higher value of DOS in the superlattice



**Fig. 23** Schematic band diagram of Ag/nc-Si:H/a-Si:H/ITO superlattice structure. The value of band gap and activation energies are obtained from transmission spectroscopy and conductivity measurements, respectively. The electron affinity of Si is taken as 4.05 eV [29]

structures as compared to single-layer a-Si:H film, which is estimated assuming no trapping of charge carriers at the interface.

The conjecture that the excess DOS in superlattice structures is due to the interface state between nc-Si:H and a-Si:H gets further support from the observed PPC in these superlattice structures which has been understood in terms of carrier trapping at the interface states; PPC (%) is found to increase with an increase in the number of interface states in these superlattice structures as discussed in PPC section. In case of SCLC measurements, the DOS for superlattice structures does not depend upon the number of layers in the given structure as these are calculated for a single pair of nc-Si:H/a-Si:H layers. Further, these values are different than those for single layer a-Si:H films as no such interface states exist in case of single-layer film. The results show that the existence of the interface states in these superlattice structures could be the reason behind the observed PPC as well as the higher DOS in these a-Si:H/nc-Si:H superlattice structures [29].

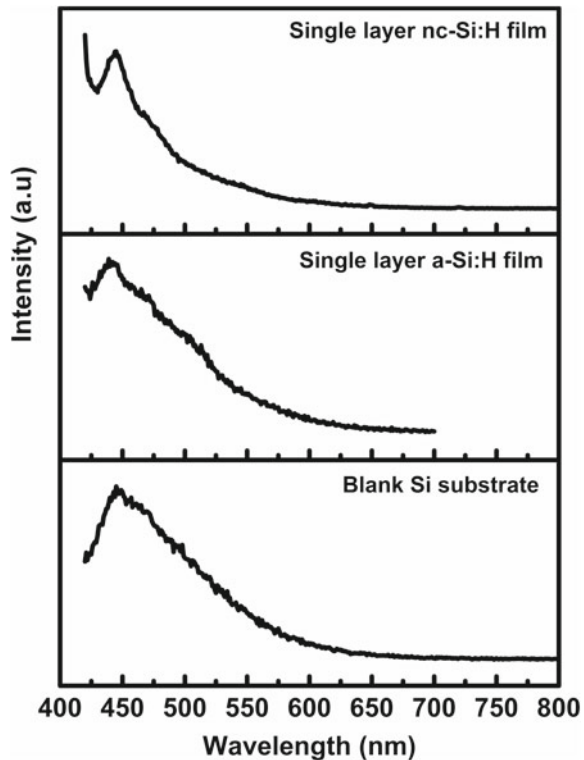
### ***3.4 Tunable Photoluminescence in nc-Si/a-Si:H Superlattice Structures***

Silicon is the most favourite material for the fabrication of microelectronic devices and integrated circuits. However, the use of silicon in photonic devices is limited due to its low band gap in IR range and also being an indirect band gap material, its photoluminescence is almost negligible. With the advancement in technology, it is sought to integrate the microelectronics and micro-photonics and optoelectronic devices on a single chip, however, indirect band gap of silicon presents a barrier to this concept. Quantum theory predicts that it is possible to tune the band gap of silicon in the visible range by suitably controlling the size of nanocrystallites and realize the integration of microelectronic and photonic devices. Several allotropes of silicon such as porous silicon and nc-Si prepared using chemical routes are known to have a strong PL signal in the visible range [24, 72–76]. However, the process of fabrication of these nanostructures restricts its use in integrated circuits and integrating these nanocrystallites of Si in a single-chip device is still a problem. Other methods for fabricating nc-Si have been explored. These include the formation of nc-Si in Si/SiO<sub>2</sub>-based superlattice structures, which can be fabricated using chemical vapour deposition route. Several superlattice structures such as nc-Si/SiO, a-Si/SiO<sub>2</sub> and Si/SiO<sub>2</sub>, a-Si/SiO<sub>2</sub> fabricated and annealed at high temperature (~1000 °C) have exhibited photoluminescence in visible range [14, 15, 25]. In all these superlattice structures small size nanocrystallites of Si could be formed, by annealing at high temperature, converting a part of a-Si or thin Si layer into nanocrystallites. All these structures have SiO<sub>2</sub> as one of the layers, which has a large band offset with silicon and also its growth requires high-temperature processing. A superlattice structure with a small band offset such as a-Si:H/nc-Si:H superlattice structure is desirable to

enhance the carrier mobility along with high optical absorption, photonic and plasmonic effects. In this section, we discuss how the photoluminescence signal can be tuned by controlling the thickness of nc-Si in a-Si:H/nc-Si superlattice structures. The structures used for these studies were fabricated by the rf-PECVD method at a low substrate temperature of 250 °C and no post-deposition annealing or any other processing was done. These structures were fabricated on undoped c-Si wafers and alkali-free borosilicate glass (Corning 1737) substrates, those fabricated on glass substrates were also used for PPC studies discussed in the earlier section. The PL spectra were recorded using solid-state laser (excitation wavelength 405 nm) with a laser power of 30 mW [13].

Figure 24 shows the PL spectra recorded for blank Si substrates as well as single-layer a-Si:H (10 nm) and nc-Si (5 nm) films. Apart from a peak at ~450 nm (2.78 eV), no photoluminescence signal is observed for either blank substrates or thick as well thin single-layer films. The peak at 2.78 eV is characteristic of SiO<sub>2</sub>, a thin layer of which is always present on the samples and substrates. The PL spectra for superlattice structures on c-Si and glass substrates, having 4 alternating layers of nc-Si and 3 layers of a-Si:H, are shown in Fig. 25 along with the spectra for an 11-layer-thick structure. The thickness of a-Si:H layer, in all these structures, is fixed at 10 nm, whereas that of nc-Si is varied between 5 and 30 nm. These structures are the same

**Fig. 24** PL spectra of single-layer a-Si:H (10 nm) and nc-Si:H (5 nm) thin films on silicon substrate and blank Si substrate [13]



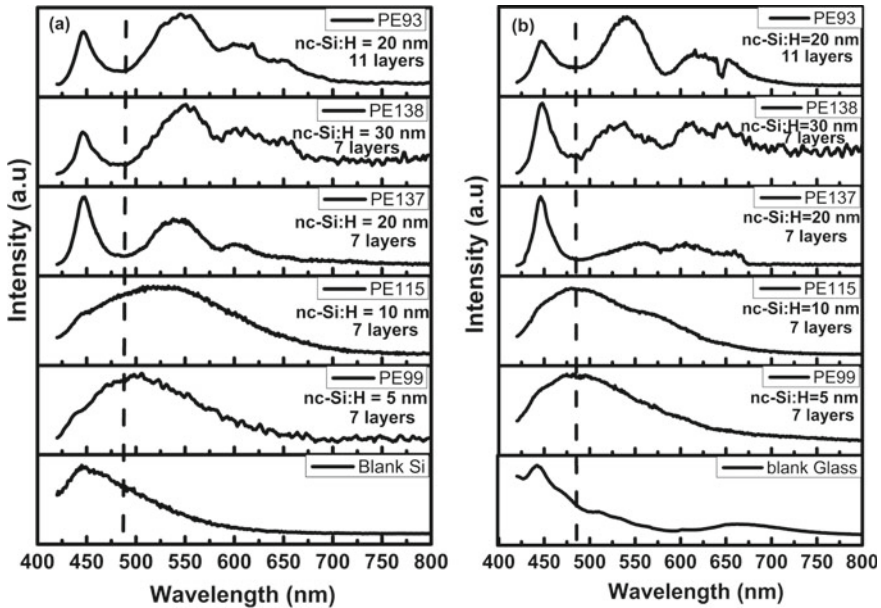
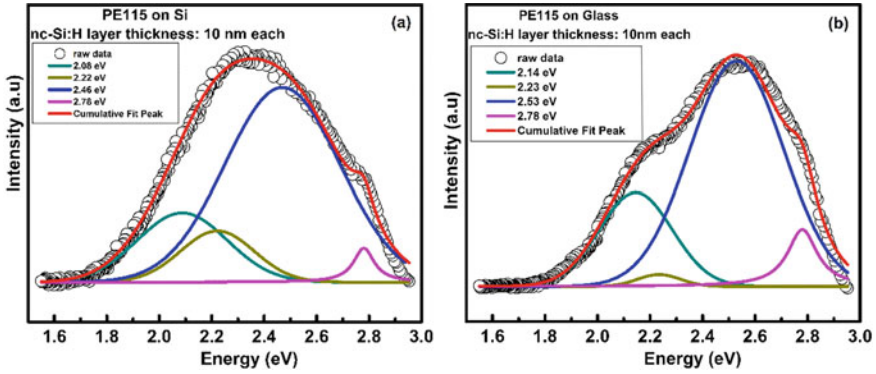


Fig. 25 PL spectra of a-Si:H/nc-Si:H superlattice structures on **a** silicon and **b** glass substrates [13]

as those used for PPC studies and were fabricated simultaneously on glass as well as c-Si substrates. As is evident from these figures, PL spectra of all these structures have a broad peak in the visible range (for nc-Si layer up to 10 nm thick) and distinct peaks when the nc-Si layer is 20–30 nm. The spectra for structures on both substrates are qualitatively identical with some change in peak intensity.

Since a broad peak in spectroscopy is often a convolution of several overlapping peaks, the PL spectra were deconvoluted to get the information about different peaks. While deconvolution, a peak at 2.78 eV corresponding to SiO<sub>2</sub> was pinned. One of the deconvoluted spectra on each substrate is presented in Fig. 26. The position of different peaks along with its full width at half maxima (FWHM) and maximum intensity is compiled in Table 6. It is observed that for all the spectra two peaks, one around 2.25 eV and another around 2.06 eV is observed. The structures with very thin nc-Si (5–10 nm) show a peak around 2.45–2.55 eV, which is replaced by a peak at 1.91 eV, when the thickness of nc-Si layers is changed to 20–30 nm. Further, in all these structures, the most intense peak is the one centred at the highest energy. In order to investigate if the peak positions also depend upon the number of layers in superlattice structures, PL measurements were also performed on a 11-layer superlattice structure having 20-nm-thick nc-Si layers. Interestingly, the positions of different peaks in the deconvoluted spectra and its FWHM were found to be the same as that for 7-layer superlattice structure with 20-nm-thick nc-Si layers, both for c-Si as well as glass substrates.

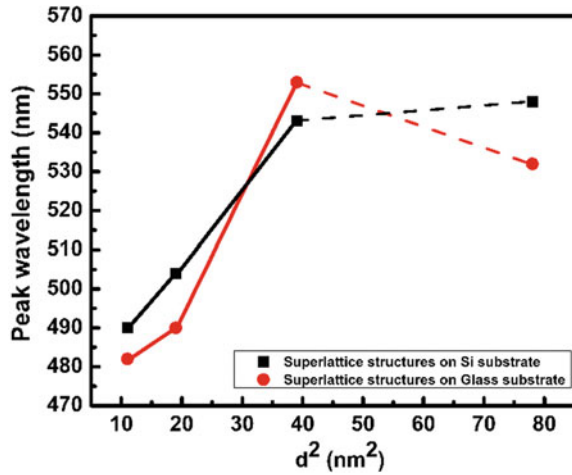


**Fig. 26** The deconvoluted PL spectra of superlattice structure films (nc-Si:H layer thickness of 10 nm) with peak position on **a** Si and **b** glass substrates

**Table 6** The PL peak position, FWHM and peak intensity of superlattice structures on glass and Si substrates [13]

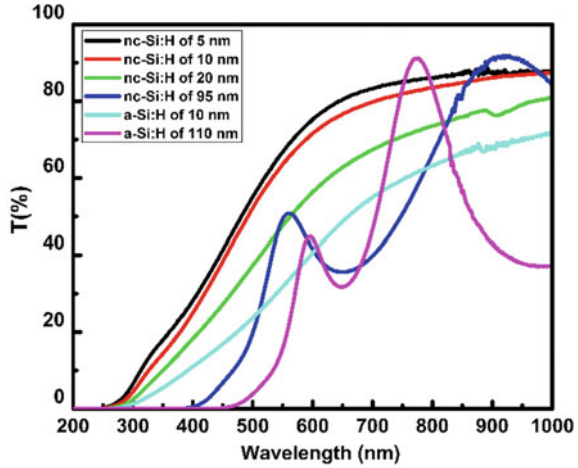
Sample no.	On Si substrate			On glass substrate		
	Peak position (eV)	FWHM (eV)	Max ht. (a.u.)	Peak position (eV)	FWHM (eV)	Max ht. (a.u.)
PE99 nc-Si:H = 5 nm (7 layer)	2.78	0.19	153	2.78	0.15	11244
	2.53	0.43	1158	2.57	0.36	35718
	2.26	0.35	382	2.34	0.24	11206
	2.09	0.44	200	2.16	0.34	13583
PE115 nc-Si:H = 10 nm (7 layer)	2.78	0.09	2145	2.78	0.13	8085
	2.46	0.51	12271	2.53	0.42	31969
	2.22	0.33	3243	2.23	0.19	1688
	2.08	0.40	4378	2.14	0.32	13319
PE137/PE93 nc-Si:H = 20 nm (7 layers/11 layers)	2.78/2.78	0.12/0.13	15738/4649	2.78/2.78	0.11/0.19	13827/13445
	2.28/2.27	0.25/0.29	10019/6079	2.24/2.30	0.33/0.23	3837/23007
	2.03/2.03	0.10/0.09	2512/2094	2.01/2.01	0.13/0.10	2602/9718
	1.91/1.91	0.24/0.16	1161/1832	1.89/1.89	0.07/0.15	2059/6673
PE138 nc-Si:H = 30 nm (7 layers)	2.77	0.11	537	2.77	0.12	694
	2.26	0.26	815	2.33	0.28	380
	2.03	0.10	352	2.03	0.13	225
	1.91	0.15	296	1.90	0.22	251

**Fig. 27** PL peak position  $\lambda$  versus  $d^2$  on silicon and Corning glass substrate [13]



It is interesting to observe a shift in PL peak position with the thickness of nc-Si layer in these multilayer structures, especially when single-layer films do not show any PL. It appears to be originated from the Si nanocrystallites embedded in the matrix of the amorphous phase in nc-Si layer, the size of which depends upon the thickness of nc-Si. In order to estimate the typical size of the nanocrystallites in nc-Si layer, single-layer nc-Si films with thickness varying between 5 and 30 nm were deposited under identical conditions and Raman measurements were performed on these thin films [50]. The Raman spectra for all these films were characterized by an intense peak near  $520\text{ cm}^{-1}$ . The peak at  $520\text{ cm}^{-1}$  corresponds to the TA mode of Si in c-Si and a shift from this position towards lower wavenumber is a measure of crystallite size [77]. The size of nanocrystallites ( $d$ ) in these thin single-layer nc-Si films are estimated to be 3.35, 4.44, 6.26 and 8.88 nm for 5-, 10-, 20- and 30-nm-thick films, respectively, which suggests a systematic increase in the size of nanocrystallites with the thickness of the films. Figure 27 shows the peak wavelength (corresponding to the most intense peak) as a function of Si nanocrystallite size ( $d$ ), estimated from Raman measurements on thin single-layer nc-Si films. It is observed that peak wavelength varies as  $d^2$ , for nc-Si layer thickness up to 20 nm for superlattice structures fabricated on Si substrates. It may appear that for structures fabricated on glass substrates, the variation is not linear, but it may be noted here that the size of nanocrystallites on glass substrates may be slightly different. For 30-nm-thick nc-Si layers, the peak wavelength does not follow this linear relation. A linear variation of peak wavelength with the size of nanocrystallites is in accordance with the quantum confinement model of Brus [78], which predicts the confinement energy of the nanocrystals to be proportional to the reciprocal of the square of the diameter of crystallites. A systematic shift in the absorption edge is also observed in the transmission spectra of these films (Fig. 28), which also suggests an increase in band gap with a decrease in thickness of the films, indicating a decrease in the size of the nanocrystallites. For 30-nm-thick nc-Si layer, small intensity peaks in PL spectra are seen due to

**Fig. 28** UV-Vis-NIR transmission spectra of single-layer a-Si:H and nc-Si:H thin films [13]



smaller size particles, however, a significant fraction of these crystallites are bigger in size and the most intense peak is observed at around 1.9 eV, which is almost same as the band gap of a-Si:H films in these structures. From these observations, the origin of high energy peaks in PL spectra appears to be due to presence of small size Si nanocrystallites in nc-Si layer, however, the same phenomenon is unable to explain the origin of low-energy (1.9 eV) peak. In order to understand the origin of this peak, we revisited the PPC data on these film, which was appreciable for superlattice structures having 30-nm-thick nc-Si layers. It appears that some of the carriers trapped in the interface states and responsible for the PPC when recombine radiatively give rise to the PL peak around 1.9 eV along with small intensity PL peaks at higher energy also, which is likely to be due to small size nanocrystallites in these nc-Si layers. When the thickness of nc-Si layer is small, the carriers are not trapped in the interface states, rather these can easily tunnel through and hence no low-energy PL peak is observed when the thickness of nc-Si layer is small [13]. These observations suggest that it is possible to tune the peak wavelength in PL spectra of nc-Si-based superlattice structures by controlling the thickness of nc-Si. The fabrication of superlattice structures thus offers a unique process of tuning the size of nanocrystallites and PL peak position.

## 4 Summary

Semiconductor superlattice structures exhibit interesting and tuneable optoelectronic properties. Most of these superlattice structures are fabricated using two different semiconductors having a large band offset at the interface. Our studies show that it is possible to fabricate the superlattice structures using different isomorphs like a-Si:H and nc-Si, which do not have much conduction band offsets but a large difference



in electrical conductivity and band gap. It is thus possible to tune the electrical transport and optoelectronic properties of these structures by carefully choosing the thickness of the individual layer. The thick individual layer structures exhibit persistent photoconductivity, whereas the thin individual layer structures can be used for tuning the photoluminescence peak, making these structures a good candidate for photonic and plasmonic applications. The interface states in these structures also have a role in controlling the optoelectronic and transport properties.

**Acknowledgments** Financial support for fabricating rf-PECVD system was received from Department of Science and Technology (DST) [Grant No. DST/TM/SERI/2K11/78(G)]; and Defence Research and Development Organization (DRDO) [Grant No. ERIP/ER/0900376/M/01/1297], New Delhi, India. The Hot wire CVD system was fabricated through the financial support from Department of Science and Technology (DST) [Grant No. DSTSR-S2-CMP-32-2003]. The study was sponsored by the Council of Scientific and Industrial Research (CSIR), New Delhi, India [80(0082)/13/EMR(II)]. We also acknowledge the Department of Physics, IIT Guwahati and Centre for Instrument Facility (CIF), IIT Guwahati for different characterization facilities and other support. We also acknowledge the fruitful discussions with (Late) Professor Satish Chandra Agarwal (IIT Kanpur) and Professor Rana Biswas (Iowa state University, Ames, USA).

## References

1. L. Esaki, R. Tsu, *IBM J. Res. Dev.* **14**, 61 (1970)
2. L. Esaki, *IEEE J. Quantum Electron.* **22**, 1611 (1986)
3. A. Wacker, *Phys. Rep.* **3**(357), 1 (2002)
4. B. Movaghar, *Semicond. Sci. Technol.* **2**, 185 (1987)
5. N. Chen, X. Li, X. Wang, S. Xie, W.Q. Tian, S. Zhang, H. Sun, *IEEE Trans. Nanotechnol.* **17**, 140 (2018)
6. H. Xu, B. Chen, F. Jin, Z. Guo, G. Gao, F. Chen, W. Wu, *Mater. Res. Express* **3**, 126403 (2016)
7. H.J. Haugan, F. Szmulowicz, K. Mahalingam, G.J. Brown, S.R. Munshi, B. Ullrich, *Appl. Phys. Lett.* **87**, 261106 (2005)
8. G.H. Döhler, *Physica Status Solidi (b)* **52**, 533 (1972)
9. G.H. Döhler, *J. Vac. Sci. Technol.* **16**, 851 (1979)
10. G.H. Döhler, H. Künzel, K. Ploog, *Phys. Rev. B* **25**, 2616 (1982)
11. M. Hundhausen, L. Ley, R. Carius, *Phys. Rev. Lett.* **53**, 1598 (1984)
12. J. Kakalios, H. Fritzsche, *Phys. Rev. Lett.* **53**, 1602 (1984)
13. A. Yadav, P. Agarwal, R. Biswas, *J. Mater. Sci.: Mater. Electron.* **30**, 4696 (2019)
14. P. Photopoulos, A.G. Nassiopoulou, D.N. Kouvatso, A. Travlos, *Mater. Sci. Eng., B* **69–70**, 345 (2000)
15. D.J. Lockwood, Z.H. Lu, J.M. Baribeau, *Phys. Rev. Lett.* **76**, 539 (1996)
16. S. Pattnaik, N. Chakravarty, R. Biswas, V. Dalal, D. Slafer, *Sol. Energy Mater. Sol. Cells* **129**, 115 (2014)
17. B.I. Sthal, Ph.D. thesis submitted to University of Rostenburg, Germany, 2008
18. D.T. Norton Jr, Ph.D. thesis submitted to University of Iowa, Iowa, 2013
19. M.B.H. Breese, D. Mangaiyarkarasi, *Opt. Express* **15**, 5537 (2007)
20. Y. Nakata, M. Asada, Y. Suematsu, *Electron. Lett.* **22**, 58 (1986)
21. Y. Nakata, M. Asada, Y. Suematsu, *Surf. Sci.* **174**, 519 (1986)
22. G.D. Mahan, L.M. Woods, *Phys. Rev. Lett.* **80**, 4016 (1998)
23. L.W. Whitlow, T. Hirano, *J. Appl. Phys.* **78**, 5460 (1995)
24. L.T. Canham, *Appl. Phys. Lett.* **57**, 1046 (1990)

25. L. Tsybeskov, K.D. Hirschman, S.P. Duttagupta, M. Zacharias, P.M. Fauchet, J.P. McCaffrey, D.J. Lockwood, *Appl. Phys. Lett.* **72**, 43 (1998)
26. M. Zacharias, L. Tsybeskov, K.D. Hirschman, P.M. Fauchet, J. Bläsing, P. Kohlert, P. Veit, J. Non-Cryst. Solids **227–230**, 1132 (1998)
27. Y.-H. So, S. Huang, G. Conibeer, M.A. Green, *Thin Solid Films* **519**, 5408 (2011)
28. A. Yadav, P. Agarwal, *Superlattices Microstruct.* **85**, 776 (2015)
29. A. Yadav, P. Agarwal, *Mater. Sci. Semicond. Process.* **61**, 5 (2017)
30. K. Ploog, G.H. Döhler, *Adv. Phys.* **32**, 285 (1983)
31. S.C. Agarwal, S. Guha, *J. Non-Cryst. Solids* **77–78**, 1097 (1985)
32. S.C. Agarwal, S. Guha, *Phys. Rev. B* **32**, 8469 (1985)
33. G.S. Paul, P. Agarwal, *J. Appl. Phys.* **106**, 103705 (2009)
34. D. Azulay, O. Millo, S. Silbert, I. Balberg, N. Naghavi, *Appl. Phys. Lett.* **86**, 212102 (2005)
35. J.Y. Lin, H.X. Jiang, *Phys. Rev. B* **41**, 5178 (1990)
36. H.X. Jiang, J.Y. Lin, *Phys. Rev. Lett.* **64**, 2547 (1990)
37. D. Cammi, C. Ronning, *Adv. Condens. Matter Phys.* **2014**, 5 (2014)
38. M.N. Islam, P.S. Dopal, H.D. Bist, S. Kumar, *Solid State Commun.* **107**, 43 (1998)
39. H.J. Queisser, D.E. Theodorou, *Phys. Rev. B* **33**, 4027 (1986)
40. Y.C.A. Shih, B.G. Streetman, *Appl. Phys. Lett.* **62**, 2655 (1993)
41. T. Ishibashi, Y. Suzuki, H. Okamoto, *Jpn. J. Appl. Phys.* **20**, L623 (1981)
42. V.K. Kononenko, H.W. Kunert, I.S. Manak, D.V. Ushakov, *J. Appl. Spectrosc.* **70**, 115 (2003)
43. S. Tong, X.N. Liu, X.M. Bao, *Appl. Phys. Lett.* **66**, 469 (1995)
44. L. Khriachtchev, S. Novikov, J. Lahtinen, *J. Appl. Phys.* **92**, 5856 (2002)
45. K. Ou, S. Wang, M. Huang, Y. Zhang, Y. Wang, X. Duan, L. Yi, *J. Lumin.* **199**, 34 (2018)
46. M.B.A.E. Wolf, Cambridge University Press, Cambridge, 1999
47. E. Hecht, *Optics*, 4th edn. (Addison Wesley, San Francisco, 2002), p. 425–500
48. A.K. Ghatak, K. Thyagarajan, *Optical electronics* (Cambridge University Press, Cambridge, 1989), p. 57
49. J.A. Pradeep, Ph.D. thesis submitted to IIT Guwahati, India, 2011
50. A. Yadav, Ph.D. thesis submitted to IIT Guwahati, India, 2018
51. A. Yadav, P. Agarwal, *Mater. Today: Proc.* **4**, 12722 (2017)
52. A. Kastalsky, J.C.M. Hwang, *Solid State Commun.* **51**, 317 (1984)
53. M. Hundhausen, L. Ley, *Phys. Rev. B* **32**, 6655 (1985)
54. F.C. Su, S. Levine, P.E. Vanier, F.J. Kampas, *Appl. Phys. Lett.* **47**, 612 (1985)
55. K.H. Jun, K.S. Lim, *J. Non-Cryst. Solids* **261**, 268 (2000)
56. V.L. Dalal, A. Madhavan, *J. Non-Cryst. Solids* **354**, 2403 (2008)
57. A. Madan, P.G. Le Comber, W.E. Spear, *J. Non-Cryst. Solids* **20**, 239 (1976)
58. G.W. Neudeck, A.K. Malhotra, *J. Appl. Phys.* **46**, 239 (1975)
59. N.B. Goodman, H. Fritzsche, H. Ozaki, *J. Non-Cryst. Solids* **35–36, Part 1**, 599 (1980)
60. W.E. Spear, P.G. Le Comber, *J. Non-Cryst. Solids* **8–10**, 727 (1972)
61. T. Tiedje, C.R. Wronski, B. Abeles, J.M. Cebulka, *Solar Cells* **2**, 301 (1980)
62. M. Hirose, T. Suzuki, G.H. Döhler, *Appl. Phys. Lett.* **34**, 234 (1979)
63. Y.T.H. Okushi, S. Yamasaki, H. Oheda, K. Tanaka, *J. Phys. Colloques* **42**, C4 (1981)
64. J. Beichler, H. Mell, K. Weber, *J. Non-Cryst. Solids* **59–60, Part 1**, 257 (1983)
65. N.M. Johnson, *J. Non-Cryst. Solids* **59–60, Part 1**, 265 (1983)
66. E. Bhattacharya, S. Guha, K.V. Krishna, D.R. Bapat, *J. Appl. Phys.* **53**, 6285 (1982)
67. H.S. Soh, C. Lee, J. Jang, M.Y. Jung, S.S. Yoo, *Appl. Phys. Lett.* **63**, 779 (1993)
68. S.B. Husain, M. Zulfequar, M.A. Majeed Khan, M. Husain, *Curr. Appl. Phys.* **4**, 445 (2004)
69. A. Bozhko, M. Shupegin, T. Takagi, *Diam. Relat. Mater.* **11**, 1753 (2002)
70. Z. Çaldıran, M. Şinoforoğlu, Ö. Metin, Ş. Aydoğan, K. Meral, *J. Alloy. Compd.* **631**, 261 (2015)
71. W.D. Boer, *J. Phys. Colloques* **42**, C4 (1981)
72. V. Lehmann, U. Gösele, *Appl. Phys. Lett.* **58**, 856 (1991)
73. W.L. Wilson, P.F. Szajowski, L.E. Brus, *Science* **262**, 1242 (1993)
74. S. Furukawa, T. Miyasato, *Phys. Rev. B* **38**, 5726 (1988)

75. D.C. Hannah, J. Yang, N.J. Kramer, G.C. Schatz, U.R. Kortshagen, R.D. Schaller, *ACS Photonics* **1**, 960 (2014)
76. O. Yukio, T. Keiji, T. Fumitaka, M. Hiroaki, K. Kenji, *Jpn. J. Appl. Phys.* **31**, L365 (1992)
77. S. Veprek, F.A. Sarott, Z. Iqbal, *Phys. Rev. B* **36**, 3344 (1987)
78. L.E. Brus, *J. Chem. Phys.* **80**, 4403 (1984)